

Quantum Radiance Fields: A Quantum-Powered Photorealistic Rendering

Yuan-Fu Yang

National Yang Ming Chiao Tung University
yfyangd@gmail.com

Min Sun

National Tsing Hua University
summin@ee.nthu.edu.tw

Abstract

Achieving photorealistic rendering of real-world scenes poses a significant challenge with diverse applications, including mixed reality and virtual reality. Neural networks, extensively explored in solving differential equations, have previously been introduced as implicit representations for photorealistic rendering. However, achieving realism through traditional computing methods is arduous due to the time-consuming optical ray tracing, as it necessitates extensive numerical integration of color, transparency, and opacity values for each sampling point during the rendering process. In this paper, we introduce Quantum Radiance Fields (QRF), which incorporate quantum circuits, quantum activation functions, and quantum volume rendering to represent scenes implicitly. Our results demonstrate that QRF effectively confronts the computational challenges associated with extensive numerical integration by harnessing the parallelism capabilities of quantum computing. Furthermore, current neural networks struggle with capturing fine signal details and accurately modeling high-frequency information and higher-order derivatives. Quantum computing's higher order of nonlinearity provides a distinct advantage in this context. Consequently, QRF leverages two key strengths of quantum computing: highly non-linear processing and extensive parallelism, making it a potent tool for achieving photorealistic rendering of real-world scenes.

1. Introduction

Traditional 3D computer vision pipelines depend on multi-view stereo algorithms for estimating sparse point clouds, camera poses, and textured meshes from 2D input views. However, re-rendering these scene representations often falls short of achieving photorealistic image quality. In stark contrast, implicit scene representations offer a substantial leap in rendering quality and can be directly supervised using 3D data through neural networks. Nonetheless, current neural networks grapple with capturing fine signal details and accurately modeling high-frequency information and higher-order derivatives, even when subjected to extensive supervision. Furthermore, achieving realistic rendering of real-world scenes using conventional computer graphics techniques is an imposing challenge, as it involves the intricate task of capturing



Figure 1: The results of volume rendering for Drums after training for 50k iterations. In comparison to the NeRF baseline [13] and AutoInt [17], QRF exhibit improved rendering efficiency and enhanced rendering quality.

nuanced appearance and geometric models. In practice, existing methods frequently produce blurry renderings due to limitations in network capacity. Generating high-resolution imagery from these representations often requires time-consuming optical ray tracing.

Recent strides in quantum computing have substantially enriched the realm of artificial neural networks. Quantum Neural Networks (QNN), a class of quantum algorithms harnessing qubits to construct adaptive neural networks, have played a pivotal role in this advancement. Quantum computing holds the promise of achieving exponential speed enhancements by executing massively parallel computations on superimposed quantum states. QNN tailored for implicit representations exhibit promise in surmounting the computational challenges that conventional techniques encounter when executed on classical computers. In this study, we employ neural rendering through quantum circuits, as shown in Figure 2. Additionally, we present a quantum volume rendering approach based on quantum integration, which has been successfully implemented on real quantum hardware. Our proposed quantum volume rendering performs the fastest among various rendering tasks and offers speed-related advantages over implementing conventional integration on digital computers. In brief, our contributions include:

(1) We introduce the first QNN-based system capable of rendering photorealistic novel views at speeds hundreds of times faster than conventional neural networks.

(2) The QRF framework is presented, comprising a collection of quantum implicit fields. For each quantum circuit, encoding circuits are learned to capture local properties, enabling high-quality rendering.

(3) We harness the power of the quantum activation function, which excels at representing signal details compared to classical activation functions in implicit

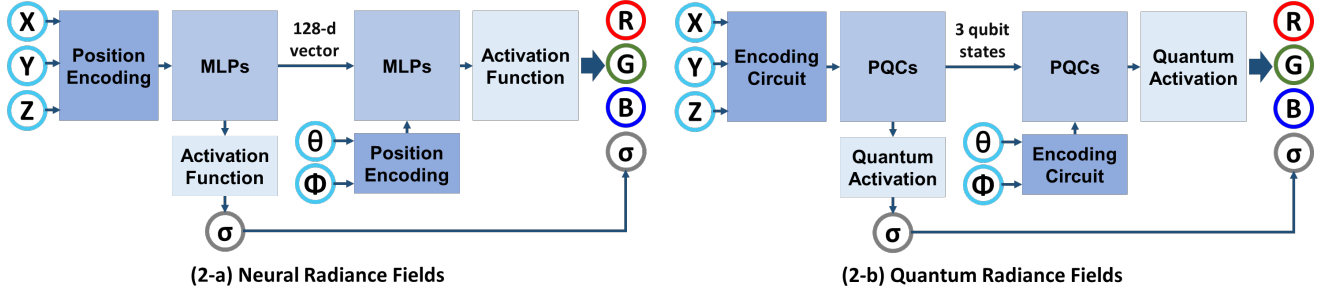


Figure 2: (2-a) NeRF architecture. Given a 3D position (x, y, z), viewing direction (θ, ϕ), NeRF produces static and transient colors (r, g, b) and transparency values (σ). (2-b): our QRF architecture replaces the same task with encoding circuit, parameterized quantum circuits, and quantum activation.

neural representations.

(4) We put forth Quantum Volume Rendering, a quantum algorithm for numerical integration, which fundamentally outperforms classical Monte Carlo integration in the context of volume rendering.

The remainder of this paper is organized as follows. In Section 2, we delve into the realm of neural scene representations, neural radiance fields, and QNN. Section 3 takes us into the domain of implicit neural representations, guided by QRF. In Section 4, we unveil our research outcomes through the lens of 2D image regression and 3D scene reconstruction. Within each task, we illustrate the advantages arising from the utilization of circuit-based QRF. Lastly, Section 5 encapsulates our study's essence, offering both a concise summary and a glimpse into potential future avenues of exploration.

2. Related Work

Neural Scene Representation. To model objects in a scene, many different scene geometry representations have been proposed. They can be divided into explicit and implicit representations. Explicit scene representations portray scenes as an assembly of geometric primitives, with their output falling into voxel-based [1,2], point-based [3,4], and mesh-based representations [5,6]. While explicit scene representations allow for the swift new perspectives generation, they are inherently constrained by the internal resolution of their representations, often resulting in blurry outcomes when dealing with high-frequency content.

To address the aforementioned challenge, numerous studies have delved into the realm of implicit neural scene representations, which enable direct inference of outputs from a continuous input space. In contrast to explicit neural scene representations, implicit neural scene representations offer the potential for 3D structure-aware, continuous, memory-efficient portrayals of shape components, objects, or entire scenes [7, 8, 9]. These representations employ neural networks to implicitly define objects or scenes and can be supervised directly using 3D data, such as point clouds, or through 2D multi-view images [10,11,12].

Neural Radiance Fields. Recent advancements in Neural Radiance Fields (NeRF) have demonstrated the capability of neural networks to acquire an implicit volumetric representation of a scene. They enable the encoding of intricate 3D environments that can be realistically rendered from novel perspectives [13]. Nevertheless, it is important to note that NeRF requires extensive point sampling along the ray to accumulate colors for achieving high-quality rendering.

Numerous techniques have emerged to accelerate NeRF. Neural Sparse Voxel Fields (NSVF) [15] utilize classical approaches such as empty space skipping and early ray termination to expedite NeRF's rendering. MetaNeRF [16] adopts standard meta-learning methods to learn initial weight parameters, leading to quicker convergence and improved reconstruction quality during test-time optimization. AutoInt [17] introduces an automatic integration framework with closed-form integral solutions, reducing the need for ray evaluations during NeRF's raymarching. DONeRF [18] enhances inference by decreasing the required number of samples along the ray. FastNeRF [19] proposes a graphics-inspired factorization technique that efficiently caches and queries data to compute pixel values in rendered images. KiloNeRF [20] represents scenes using numerous smaller MLP instead of a single large-capacity MLP, facilitating the use of smaller and faster evaluation MLP. DS-NeRF [21] employs depth as an additional source of supervision to regularize NeRF's geometry learning and improve training. Cheng Sun and Min Sun et al. [22] present a super-fast convergence method for reconstructing per-scene radiance fields, drastically reducing training time from hours to just 15 minutes while maintaining quality on par with NeRF.

Quantum Neural Networks. QNN represent a nascent domain that amalgamates the computational advantages introduced by quantum computing with advancements beyond classical computation [23]. These networks not only enhance algorithmic efficiency but also exhibit a heightened probability of converging to the global minimum when seeking solutions [24]. At their core,

quantum computing principles draw inspiration from quantum physics, encompassing concepts like superposition, entanglement, and interference. A qubit system has the capacity to hold multiple bits of information concurrently, thus unlocking the potential for extensive parallelism [25].

3. Method

To achieve real-time, cinematic-quality rendering of concise neural representations for generated content, we adopt a QNN-based neural raymarching approach inspired by NeRF [13], which employs MLPs to encode densities and colors at continuous 3D positions within the scene. Drawing inspiration from DOnERF [18], we adopt a compact local sampling strategy for scene representation. This strategy enables the raymarching-based neural representation to focus on essential samples around the surface region, thereby reducing the utilization of qubits in simulated environments and quantum computers. In the upcoming sections, we provide an overview of the NeRF baseline model in Sec. 3.1, detail our QRF in Sec. 3.2, introduce the Quantum Activation Function in Sec. 3.3, and present Quantum Volume Rendering in Sec. 3.4.

3.1. Baseline Model

In the NeRF, the scene representation is accomplished by a neural network, denoted as f_θ with parameter θ_n , designed to capture the 3D volumetric information. NeRF's neural network, $f_\theta: (p, d) \rightarrow (c, \sigma)$, maps a 3D position $p \in \mathbb{R}^3$ and a light direction $d \in \mathbb{R}^2$ to the color value c and transparency σ . The architecture of f_θ is thoughtfully structured to ensure that only the color c relies on the viewing direction d . This design choice promotes the learning of consistent scene geometry. In the preliminary deterministic preprocessing step, both x and d undergo a transformation via positional encoding, represented as γ . This encoding strategy facilitates the learning of high-frequency details in the data.

To render an individual image pixel, a ray is projected from the camera's center through the pixel and into the scene, with the direction of this ray denoted as d . Multiple 3D positions (p_1, \dots, p_k) are sampled along the ray between the near and far boundaries defined by the camera parameters. At each position p_i along the ray and for the given ray direction d , the neural network f_θ is evaluated, producing color c_i and transparency σ as intermediate outputs. These intermediate results are subsequently integrated to yield the final pixel color \hat{c} as follows:

$$\hat{c} = \sum_i^K T_i (1 - e^{(-\sigma_i \delta_i)}) c_i \quad (1)$$

where $T_i = e^{-\sum_{j=i}^{i-1} \sigma_j \delta_j}$ is the transmittance and $\delta_j = (p_{i+1} - p_i)$ is the distance between samples. As f_θ is

contingent on the ray direction, NeRF has the capacity to capture viewpoint-dependent effects, including specular reflections. This capability marks a significant dimension in which NeRF outperforms traditional 3D representation.

3.2. Quantum Radiance Fields

The QRF is implemented by a series of quantum circuits built into the continuous-variable architecture. It consists of three consecutive parts (as shown in Figure 2). An encoding circuit encodes the classical data into the states of the qubits, followed by a parameterized quantum circuits (PQCs), which is used to transform these states to their optimal location on the Hilbert space. Lastly, quantum activation is employed to perform nonlinear mapping on the input, introducing nonlinear factors into the neural networks. This augmentation enables the neural networks to more effectively capture the color and transparency attributes at each position along the ray.

3.2.1 Encoding Circuit

The encoding circuit is used to encode the classical data into the physical states of Hilbert space for quantum computing [26], which is critical to the success of QNN. Quantum encoding can be thought of as loading a data point $x \in X$ from memory into a quantum state so that it can be processed by a QNN. The loading is accomplished by encoding from the set X to the n -qubit quantum state D_n . Numerous QNN papers [27, 28, 29] have advocated wavefunction encoding with $n = \log_2 2N$. This approach offers substantial space savings, albeit at the expense of a significant increase in computational time. In essence, a quantum state composed of $\log_2 2N$ qubits can represent a data point with N features, but the preparation of such a quantum state demands $O(2^n)$ time. Recent researchers [30, 31, 32] have explored alternative methods, such as angle encoding, which efficiently encodes classical data into quantum states, effectively mitigating the time complexity concerns associated with wave encoding.

Angle Encoding. Angle encoding makes use of rotation gates to encode classical information $x_k \in \mathbb{R}^N$ without any normalization condition. Angle encoding can be constructed using a single rotation with angle θ_k (normalized to be in $[-\pi, \pi]$) for each qubit, and can therefore encode N features with N qubits. Angle encoding consists in the following transformation:

$$S_k |0\rangle = \bigotimes_{k=0}^N \cos(\theta_k) |0\rangle + \sin(\theta_k) |1\rangle \quad (2)$$

where the circuit starts with the $|0\rangle$ state and proceeds to encode a data point x_k using a circuit S_k . The number of qubits, denoted as N , equals the dimension of the vector x_k that is being encoded. Angle encoding is remarkably straightforward and characterized by a depth of only 1. The primary advantage of angle encoding lies in its operational efficiency: It requires only a constant number of parallel

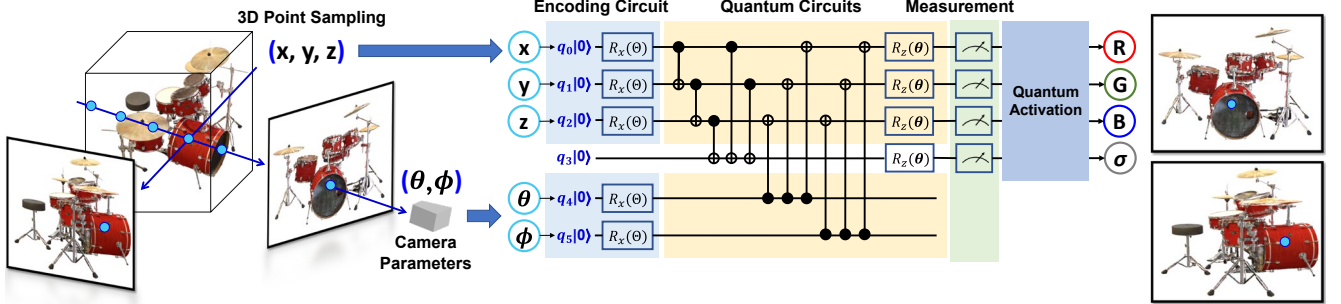


Figure 3: Quantum Radiance Fields with encoding circuits and quantum circuits produces colors (r, g, b) and transparency values (σ) given a 3D position (x, y, z) and viewing direction (θ, ϕ). Similar to the NeRF architecture, QRF enforces that the predicted σ is independent of view direction. Note that this schematic is a simplified quantum circuit with only 4 rotation gates around the z axis.

operations, regardless of the quantity of data values that need to be encoded. However, from a qubit perspective, this approach is not optimal since each component of the input vector necessitates a dedicated qubit [40].

Dense Angle Encoding. Angle encoding can be slightly generalized to encode two features per qubit by exploiting the relative phase degree of freedom [41]. We refer to this as the dense angle encoding and include a definition below:

$$|x\rangle = \bigotimes_{k=1}^{N/2} \cos(\theta_{2k}) |0\rangle + e^{2\pi k x_{2k}} \sin(\pi\theta_{2k}) |1\rangle \quad (3)$$

where x is a feature vector $x = [x_1, \dots, x_N]^T \in \mathbb{R}^N$, the dense angle encoding maps $x \rightarrow E(x)$. Dense encoding is derived by extending the above formula into two features using relative phase degrees of freedom. It exploits the additional property of relative phase qubits to encode N data points using only $N/2$ qubits.

3.2.2 Parametrized Quantum Circuits.

Parametrized Quantum Circuit is composed of a set of parameterized single and controlled single qubit gates. The parameters are iteratively optimized by a classical optimizer to attain a desired input-output relationship. A block-diagonal approximation to the Fubini-Study metric tensor of a PQCs can be evaluated on quantum hardware. In general, an n qubits PQCs can be written as:

$$u(\hat{\theta})|\varphi_0\rangle = \left(\prod_{\ell=1}^k W_\ell u_\ell(\theta_\ell) \right) |\varphi_0\rangle \quad (4)$$

where φ_0 is the initial quantum state, m is the maximum circuit depth, W_ℓ is the non-parameterized quantum gate at ℓ -th layer, $u_\ell(\theta_\ell)$ is the parametrized quantum gate with parameters $\{\theta_0, \theta_1, \dots, \theta_k\}$ at ℓ -th layer, which is a sequence consisting of parameterized qubit gates. Herein, the form of $u_\ell(\theta_\ell)$ is variable and accords with any physical constraint such as highly limited connectivity between physical qubits.

To achieve better entanglement of the qubits before appending nonlinear operations, the n qubits PQCs has n repeated layers in our model. In order to provide

computational speedup by orchestrating constructive and destructive interference of the amplitudes in quantum computing, we constructed m rotation gates on the n qubits PQCs as our basic quantum circuit, which can be written as:

$$\left(\prod_{\ell=1}^n \left(\bigotimes_{j=0}^m CNOT_{i,i+1} R(\theta_{i+n \times j}) \right) \right) \quad (5)$$

where $CNOT_{i,i+1}$ represents $CNOT$ gate as the control qubit. $R(\theta_{i+n \times j})$ represents the rotation gate along each of the X, Y, and Z-axis. $\theta_{i+n \times j}$ is adjustable parameter of rotation gates R . With the Pauli matrix, we can define single-qubit rotation along each of the X, Y, and Z-axis as:

$$R_x(\theta) = e^{-i\frac{\theta}{2}\sigma_x} = \begin{bmatrix} \cos(\theta/2) & -i\sin(\theta/2) \\ -i\sin(\theta/2) & \cos(\theta/2) \end{bmatrix} \quad (6)$$

$$R_y(\theta) = e^{-i\frac{\theta}{2}\sigma_y} = \begin{bmatrix} \cos(\theta/2) & -\sin(\theta/2) \\ \sin(\theta/2) & \cos(\theta/2) \end{bmatrix} \quad (7)$$

$$R_z(\theta) = e^{-i\frac{\theta}{2}\sigma_z} = \begin{bmatrix} e^{-i\frac{\theta}{2}} & 0 \\ 0 & e^{i\frac{\theta}{2}} \end{bmatrix} \quad (8)$$

where $\{\sigma_x, \sigma_y, \sigma_z\}$ is Pauli matrices. The operation of $R(\theta)$ can be modified by changing parameters θ . Thus, the output state can be optimized to approximate the wanted state. By optimizing the parameters, the general PQCs tries to approximate arbitrary states so that it can be used for different specific molecules. The goal of PQCs is to solve an optimization problem encoded into a cost function:

$$\theta^* = \underset{\theta \in C}{\operatorname{argmin}}(\langle \psi(\theta) | H | \psi(\theta) \rangle) \quad (9)$$

where H is the Hamiltonian with the ground energy to seek. As parameters θ are continuous, many gradient-based optimization algorithms can be used to find the optimal ones. Figure 3 shows an example of Parametrized Quantum Circuit with $n=6$ and $m=4$. Four qubits use the rotation gate $R(\theta)$ by the angle θ around z-axis on the Hilbert space, and $CNOT$ gate is used for 2 specific qubits.

3.3. Quantum Activation Function

Recent implicit neural representations are built on ReLU-based multilayer perceptron. These architectures lack the capacity to represent the fine details in the underlying signal, and they often do not represent the derivative of the target signal well. This is partly due to the fact that ReLU networks are piecewise linear, and their second derivatives are zero everywhere, so they cannot model the information contained in the higher-order derivatives of natural signals. To address these limitations, we leverage quantum activation functions, which can better represent details in signals than ReLU-MLP for implicit neural representations.

We apply a multi-step quantum approach by selecting the ReLU's solution for positive values $R(z)_{ReLU}$, and the LReLU's solution for negative values $R(z)_{LReLU}$ [42]. By applying the quantum principle of entanglement, the tensor product of the two candidate Hilbert state spaces from H_{ReLU} and H_{LReLU} was performed as:

$$H_{ReLU} \otimes H_{LReLU} \quad (10)$$

The quantum entanglement in Eq. 10 allows to overcome the limitation of the ReLU being dying for negative inputs. The resulting state in the blended system is described by:

$$|\varphi\rangle_{ReLU} \otimes |\varphi\rangle_{LReLU} \quad (11)$$

In an entangled or inseparable state, the formulation of product states of Quantum ReLU (QReLU) can be generalized as:

$$|\varphi\rangle_{QReLU} = \sum_{ReLU, LReLU} |0\rangle|1\rangle_{ReLU} \otimes |0\rangle|1\rangle_{LReLU} \quad (12)$$

where keeping output for positive values in the QReLU, but with the added novelty of the entangled solution for negative values. This fits complicated signals, such as natural images and 3D shapes, and their derivatives robustly.

3.4. Quantum Volume Rendering

Conventional implicit neural representations represent a scene as an implicit function $F_\theta(p, v) \rightarrow (c, \omega)$, where θ are parameters of an underlying neural network [13]. It evaluate a volume rendering integral to compute the color of camera ray $p(z) = p_0 + z \cdot v$ as:

$$c(p_0, v) = \int_0^\infty \omega(p(z)) \cdot c(p(z), v) dz \quad (13)$$

where $\int_0^\infty \omega(p(z)) dz = 1$, c is the scene color, ω is the probability density at spatial location p and ray direction v . $c(p_0, v)$ describes the scene color c and its probability density ω at spatial location p and ray direction v .

Volume rendering methods estimate the integral

$c(p_0, v)$ by densely sampling points on each camera ray and accumulating the colors and densities of the sampled points into a 2D image as:

$$c(p_0, v) \approx \sum_{i=n}^N \left(\prod_{j=1}^{i-1} \alpha(z_j, \Delta_j) \right) \cdot (1 - \alpha(z_i, \Delta_i)) \cdot c(p(z_i), v) \quad (14)$$

where $\alpha(z_i, \Delta_i) = \exp(-\sigma(p(z_i), v))$, and $\{\sigma(p(z_i))\}_{i=1}^N$ are the colors and the volume densities of the sampled points.

Although volume rendering offer unprecedented image quality, they are also extremely slow and memory inefficient. This is because volume rendering methods need to sample a large number of points along the rays for color accumulation to achieve high quality rendering. Previous works only considered non-empty voxels for raymarching and reduce the number of samples per ray [15, 18]. However, for scenes with high depth and complexity, this works will result in longer evaluation time and lower rendering quality.

Volume rendering is essentially a numerical integration problem in each pixel, which is commonly done by Monte Carlo integration on classical computers. In this paper, we propose the quantum ray tracing, a quantum algorithm for numerical integration that is fundamentally superior to classical Monte Carlo integration. Furthermore, we apply Grover's search [33] to design clever algorithms to take full advantage of quantum parallelism. Given a ray tracing oracle that implements the following transformations:

$$O_f(pixel, channel): \sum_{j=0}^{N-1} x_j |j\rangle \rightarrow \sum_{j=0}^{N-1} x_j |j\rangle |f(j)\rangle \quad (15)$$

where *pixel* and *channel* (R, G or B) are classical parameters, j plays the role of ray identity, and $f(j)$ is a real number that stands for the ray energy. In the rest of this paper f is specified as the function that maps ray j to ray energy. The oracle can trace $N = 2n$ paths simultaneously, and the final color we hope to write to the corresponding pixel and channel is the average of those energies $\frac{1}{N} \sum_{j=0}^{N-1} f(j)$. Suppose those real numbers $f(j)$ are stored in a fixed-point format with integer bit length b_0 and total bit length b , we can transfer the estimation problem of Eq. 15 into quantum counting by constructing a Boolean function:

$$g(j, k) = \begin{cases} 1, & f(j) \geq 2^{b_0 - b_k} \\ 0, & f(j) < 2^{b_0 - b_k} \end{cases} \quad (16)$$

where $k = (0, 1, \dots, 2^b - 1)$. The phase oracle O_g for g in Grover's search as:

$$O_g: \sum_{j,k} |j\rangle|k\rangle \rightarrow \sum_{j,k} (-1)^{g(j,k)} |j\rangle|k\rangle \quad (17)$$

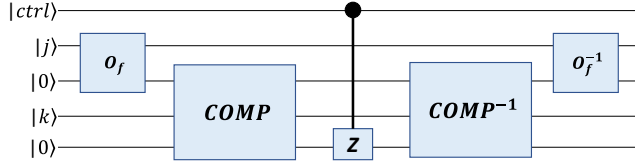


Figure 4: The construction of controlled- O_g

To construct O_g , we need a comparison gate that performs the comparison operation $COMP$ on the two integers $2^{b-b_0}f(j)$ and k ,

$$COMP: \sum_{j,k} |f(j)\rangle|k\rangle \rightarrow \sum_{j,k} |f(j)\rangle|k\rangle|g(j,k)\rangle \quad (18)$$

The O_g gate can be constructed as Figure 4. The quantity $\sum_{j,k} g(j,k)$ can be estimated by quantum counting algorithm. In the paper we assume one call to O_f quantum ray tracing takes the same samples as tracing one path in classical numerical integration. We evaluate the cost of classical path tracing by the number of ray paths N_c , as the noise comes mostly from the Monte Carlo integration. And in quantum ray tracing, the time cost is evaluated by the number of queries N_q to the ray tracing oracle O_f . The quantum integration has a convergence rate of $O(1/N_q)$, hence has a quadratic speedup over classical Monte Carlo integration with convergence rate of $O(1/\sqrt{N_c})$.

4. Results

4.1. Task

2D Image Regression. We train a QNN to regress from 2D input pixel coordinates to the corresponding RGB values of an image (as shown in Figure 5). We consider two different distributions \mathcal{H} : face images (CelebA [34]) and natural images (Div2K [35]). Given a sampled image $\mathbf{h} \sim \mathcal{H}$, we resize all images to 256×256 as observations for network weights θ in the optimization inner loop. At each inner loop step, the entire image is reconstructed and used to compute the loss. We then compare the classical MLP and QNN over these two distributions.

3D Scene Representation. The goal of 3D scene representation is to generate a novel view of the scene from

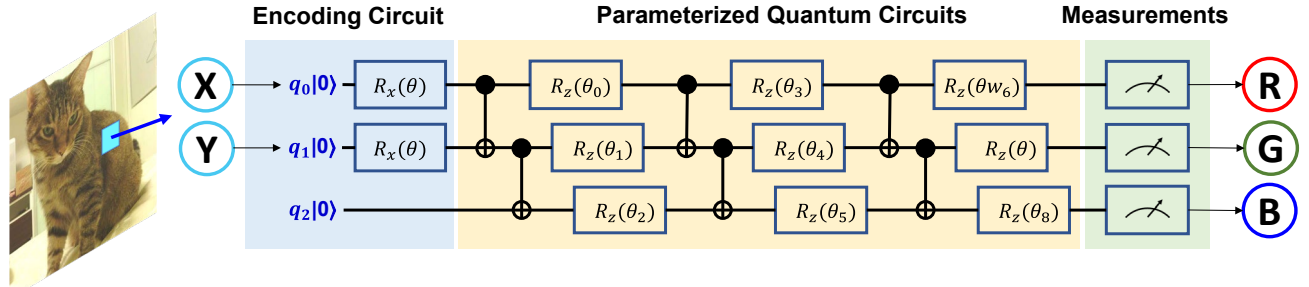


Figure 5: Quantum Implicit Neural Representations on 2D image regression with Encoding Circuit and PQS (n=3, m=3)

a set of reference images. We validate our QRF through an extensive series of ablation studies and comparisons to recent techniques for accelerating NeRF. We evaluate our method on three inward-facing datasets:

(1) Synthetic-NeRF [13]: The Synthetic-NeRF dataset consists of 360-degree views of complex objects in 8 scenes, where each scene has a central object with 100 inward facing cameras distributed randomly on the upper hemisphere. The images are 800×800 with provided ground truth camera poses.

(2) Synthetic-NSVF [15]: The Synthetic-NSVF contains 8 objects synthesized by NSVF. Strictly following the settings of NSVF, we set the image resolution to 800×800 pixels and let each scene have 100 views for training and 200 views for testing.

(3) Tanks & Temples [36]: The Tanks and Temples is a real-world dataset containing 5 scenes of real objects captured by an inward-facing camera surrounding the scene. Each scene contains between 152-384 images of size 1920×1080 .

4.2. Implementation

The principal baseline for our experiments is NeRF [13]. We report the results of the original NeRF implementation, as well as the reimplementation in Jax (JaxNeRF) [14]. We also compare two older methods, Scene Representation Network (SRN) [7] and Neural Volume [8], as well as five recent papers introducing NeRF accelerations, Neural Sparse Voxel Field (NSVF) [15], AutoInt [17], FastNeRF [19], KioNeRF [20] and Depth-supervised NeRF (DS-NeRF) [21]. To evaluate QRF, we focus on two competing requirements of scene representations: quality of the generated images, and efficiency of the image generation. To quantify the rendering quality, we rely on three metrics:

(1) Peak Signal to Noise Ratio (PSNR): A classic metric to measure the corruption of a signal.

(2) Structural Similarity Index Measure (SSIM) [37]: A perceptual image quality assessment based on the degradation of structural information.

(3) Learned Perceptual Image Patch Similarity (LPIPS) [38]: A perceptual metric based on the deep features of a trained network that is more consistent with human judgement.

where higher PSNR, SSIM and lower LPIPS is most

desirable. We train both the NeRF baseline and QRF for a high number of iterations to find the limits of the representation capabilities of the respective architectures. We train each model for 350k iterations. For the classical scene representation, we train it in 48 hours using 2 Tesla V100 GPUs. For our 2D quantum representations and QRF model, we train it with Borealis, a photonic quantum processor from Xanadu that can be programmed and entangled. The inference time performance is measured on a Tesla V100 for classical NeRF and a Borealis for QRF.

4.3. Ablation Study

We use Div2K dataset [35] and the Drums scene of Synthetic-NeRF [13] to conduct the ablation experiments. The strategy of Activation Function, Encoding Circuit, and Quantum Circuit are discussed in this section.

Activation Function. We first compare the performance of the classical activation function and the quantum activation function in the 2D image regression and 3D scene representation task. We use Rectified Linear Unit (ReLU), Exponential Linear Unit (ELU), Smooth ReLU (SoftPlus), SIREN [9] as the classical activation function, and QReLU as quantum activation function. For 2D image regression, we train an MLP with 4 layers/256 channels and apply sigmoid activation to the output for each task. For 3D scene representation, we train baseline NeRF with 6 layers/256 channels and apply positional encoding to the input coordinates. Table 1 shows that when the QReLU function serves as the activation function for each task, it outperforms the state-of-the-art activation function, which indicates that the quantum activation function has better convergence.

Table 1: Ablation Study of activation function from the Div2K and Synthetic-NeRF dataset.

Task		2D Image Regression			3D Scene Representation		
Datasets		Div2K Dataset [35]			Synthetic-NeRF [13]		
Evaluate Metrics		PSNR	SSIM	LPIPS	PSNR	SSIM	LPIPS
Classical AF	ReLU	32.89	0.961	0.044	24.85	0.812	0.208
	ELU	23.12	0.380	0.258	-	-	-
	Softplus	19.37	0.273	0.482	-	-	-
	SIREN	36.92	0.970	0.021	26.44	0.907	0.179
Quantum AF	QReLU	38.43	0.971	0.016	27.12	0.919	0.168

Encoding Circuit and Quantum Circuit. We validate our QRF on our quantum system using various encoding circuits and quantum circuits. We use circuit-5/6/16/17 provided by Sukin Sim et al. [39], which has better expressive ability and entanglement ability, as the quantum circuit baseline. In addition, we adopt general qubit encoding, wavefunction encoding, angle encoding, and

dense angle encoding as our encoding circuit strategy. More details about our quantum circuit and encoding circuit can be found in the supplemental.

The ablation results yield many significant findings (as shown in Table 2). First, circuit-5 and circuit-6 are the fully connected graph arrangement of qubits which led to both favorable expressibility and entangling capability. Therefore, the network model with circuit-5 and circuit-6 has a high PSNR regardless of the encoding circuit used. Second, circuit-5 and circuit-16 with controlled Z-rotation (CRz) gates outperform circuit-6 and circuit-17, respectively. This is because the CRz operations in the entangling block commute with each other and thus the effective unitary operation comprised of CRz gates can be expressed using unique generator terms that are fewer than the number of parameters for these gates.

Table 2: Ablation Study of encoding circuit and quantum circuit from the Synthetic-NeRF dataset.

Evaluate Metrics	Encoding Circuit	Quantum Circuit			
		5	6	16	17
PSNR	General Qubit Encoding	26.52	26.33	25.52	24.82
	Wavefunction Encoding	26.58	26.39	25.58	24.88
	Angle Encoding	26.98	26.80	25.99	25.29
	Dense Angle Encoding	27.33	27.15	26.33	25.64
SSIM	General Qubit Encoding	0.893	0.875	0.833	0.809
	Wavefunction Encoding	0.880	0.885	0.838	0.820
	Angle Encoding	0.911	0.900	0.860	0.832
	Dense Angle Encoding	0.921	0.915	0.873	0.838
LPIPS	General Qubit Encoding	0.183	0.183	0.195	0.211
	Wavefunction Encoding	0.182	0.189	0.195	0.208
	Angle Encoding	0.175	0.176	0.188	0.206
	Dense Angle Encoding	0.169	0.176	0.183	0.199

4.4. Experiment Results

2D Image Regression. We first compare the performance between classical MLP and QNN model in the task of 2D image regression. According to the ablation study result, we use QReLU as the activation function, dense angle encoding as the encoding circuit, and circuit-5 as our parameterized quantum circuit. Table 3 shows that our proposed quantum model has significant advantages in each evaluate metric.

3D Scene Representation. We leverage the same approach (utilizing QReLU, dense angle encoding, and circuit-5) as QNN to construct the QRF architecture. As illustrated in Table 4, our findings demonstrate that QRF

Table 3: Quantitative comparisons for 2D image regression. Compared with classical MLP, our proposed QNN model outperforms in the rendering quality.

Datasets	CelebA [33]			Div2K Dataset [34]		
	PSNR	SSIM	LPIPS	PSNR	SSIM	LPIPS
Classical MLP	30.67	0.945	0.112	32.89	0.961	0.044
QNN	33.71	0.963	0.038	36.36	0.969	0.027

inference outperforms NeRF by a staggering factor of over 2000, even surpassing most alternative methods, with the exception of FastNeRF. This remarkable acceleration in QRF’s inference speed can be attributed to its efficient caching and subsequent query computation for pixel values, achieved through a factorization approach. Moreover, QRF excels in all image quality metrics, making it a standout performer. Our method does not directly tackle the issue of training speed. We propose addressing the training speed of NeRF models by exploring techniques such as initializing through Meta Learning [16] or reconstructing the per-scene radiance field via DVGO NeRF [22].

Table 4: Quantitative results on each scene from the Synthetic-NeRF [13], Synthetic-NSVF [15], and Tanks and Temples [36]. We highlight the top 3 results in each column are color coded as **Top 1**, **Top 2** and **Top 3**.

Dataset	Synthetic-NeRF [13]				Synthetic-NSVF [15]				Tanks and Temples [36]			
	PSNR	SSIM	LPIPS	FPS	PSNR	SSIM	LPIPS	FPS	PSNR	SSIM	LPIPS	FPS
SRN [7]	22.26	0.846	0.170	0.909	24.33	0.882	0.141	1.304	24.10	0.847	0.251	0.250
Neural Volumes [8]	26.05	0.893	0.160	3.330	25.83	0.892	0.124	4.778	23.70	0.834	0.260	1.000
NeRF [13]	31.01	0.947	0.081	0.023	30.81	0.952	0.043	0.033	25.78	0.864	0.198	0.007
JaxNeRF [14]	31.69	0.953	0.049	0.045	31.49	0.958	0.026	0.065	27.94	0.904	0.168	0.013
NSVF [15]	31.75	0.953	0.047	0.815	35.18	0.979	0.015	0.095	28.42	0.907	0.153	0.163
AutoInt [17]	25.55	0.911	0.170	0.380	26.63	0.916	0.090	0.545	22.28	0.766	0.278	0.116
DoNeRF [18]	32.50	0.957	0.037	5.635	32.29	0.962	0.027	8.085	27.02	0.805	0.174	1.715
FastNeRF [19]	29.97	0.941	0.053	172.42	29.78	0.946	0.083	224.71	24.92	0.792	0.213	47.67
KioNeRF [20]	31.02	0.950	0.051	38.46	33.37	0.970	0.020	55.07	28.41	0.910	0.091	11.68
QRF	32.65	0.960	0.029	47.26	35.44	0.980	0.014	67.70	29.65	0.820	0.085	14.36

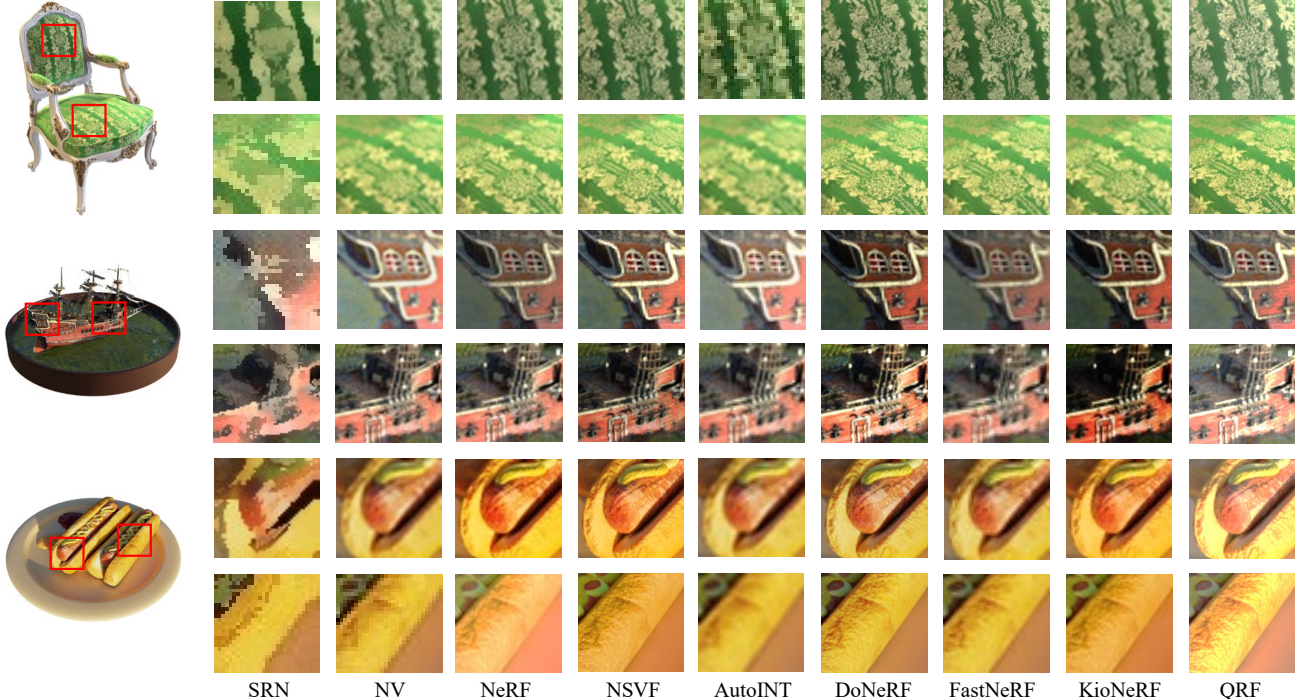


Figure 6: Qualitative comparisons on Synthetic-NeRF [13]. We compare classical implicit representation, NeRF, NeRF accelerations, and our proposed method. On this dataset, we find that our method better recovers the fine details in the scene. The results are similar in other datasets, please refer to our supplementary for more details.

References

[1] Zhirong Wu, Shuran Song, Aditya Khosla, Fisher Yu, Linguang Zhang, Xiaoou Tang, and Jianxiong Xiao, "3D ShapeNets: A deep representation for volumetric shapes", *Computer Vision and Pattern Recognition (CVPR)*, 2015. [2](#).

[2] Jiajun Wu, Chengkai Zhang, Xiuming Zhang, Zhoutong Zhang, William T. Freeman, and Joshua B. Tenenbaum, "Learning shape priors for single-view 3D completion and reconstruction", *European Conference on Computer Vision (ECCV)*, 2018. [2](#).

[3] Haoqiang Fan, Hao Su, and Leonidas Guibas, "A point set generation network for 3D object reconstruction from a single image", *Computer Vision and Pattern Recognition (CVPR)*, 2017. [2](#).

[4] Charles R. Qi, Hao Su, Kaichun Mo, and Leonidas J. Guibas, "PointNet: Deep learning on point sets for 3D classification and segmentation", *Computer Vision and Pattern Recognition (CVPR)*, 2017. [2](#).

[5] Kan Guo, Dongqing Zou and Xiaowu Chen, "3D mesh labeling via deep convolutional neural networks", *ACM Trans. on Graphics (SIGGRAPH)*, 2015. [2](#).

[6] Pengyu Wang, Yuan Gan, Panpan Shui, Fenggen Yu, Yan Zhang, Songle Chen, and Zhengxing Sun, "3D shape segmentation via shape fully convolutional networks", *Computers & Graphics*, 2017. [2](#).

[7] Vincent Sitzmann, Michael Zollhöfer and Gordon Wetzstein, "Scene representation networks: Continuous 3d-structure-aware neural scene representations", *Neural Information Processing Systems (NeurIPS)*, 2019. [2, 6, 8](#).

[8] Stephen Lombardi, Tomas Simon, Jason Saragih, Gabriel Schwartz, Andreas Lehrmann and Yaser Sheikh, "Neural volumes: Learning dynamic renderable volumes from images", *ACM Transactions on Graphics (TOG)*, vol. 38, no. 4, pp. 65-65, 2019. [2, 6, 8](#).

[9] Vincent Sitzmann, Julien N.P. Martel, Alexander W. Bergman, David B. Lindell and Gordon Wetzstein, "Implicit neural representations with periodic activation functions", *Neural Information Processing Systems (NeurIPS)*, 2020. [2, 7](#).

[10] Shunsuke Saito, Zeng Huang, Ryota Natsume, Shigeo Morishima, Angjoo Kanazawa and Hao Li, "PIFu: Pixel-aligned implicit function for high-resolution clothed human digitization", *International Conference on Computer Vision (ICCV)*, 2019. [2](#).

[11] Michael Oechsle, Lars Mescheder, Michael Niemeyer, Thilo Strauss and Andreas Geiger, "Texture fields: Learning texture representations in function space", *International Conference on Computer Vision (ICCV)*, 2019. [2](#).

[12] Lior Yariv, Yoni Kasten, Dror Moran, Meirav Galun, Matan Atzmon, Ronen Basri, et al., "Multiview neural surface reconstruction by disentangling geometry and appearance", *Neural Information Processing Systems (NeurIPS)*, 2020. [2](#).

[13] Ben Mildenhall, Pratul P. Srinivasan, Matthew Tancik, Jonathan T. Barron, Ravi Ramamoorthi and Ren Ng, "NeRF: Representing scenes as neural radiance fields for view synthesis", *European Conference on Computer Vision (ECCV)*, 2020. [1, 2, 3, 5, 6, 8](#).

[14] Boyang Deng, Jonathan T. Barron, and Pratul P. Srinivasan, "JaxNeRF: an efficient JAX implementation of NeRF", <http://github.com/google-research/google-research/tree/master/jaxnerf>, 2020. [6, 8](#).

[15] Lingjie Liu, Jiatao Gu, Kyaw Zaw Lin, Tat-Seng Chua and Christian Theobalt, "Neural sparse voxel fields", *Neural Information Processing Systems (NeurIPS)*, 2020. [2, 5, 6, 8](#).

[16] Matthew Tancik, Ben Mildenhall, Terrance Wang, Divi Schmidt, Pratul P. Srinivasan, Jonathan T. Barron, and Ren Ng, "Learned initializations for optimizing coordinate-based neural representations", *Conference on Computer Vision and Pattern Recognition (CVPR)*, 2021. [2, 8](#).

[17] David B. Lindell, Julien N. P. Martel, and Gordon Wetzstein, "AutoInt: Automatic integration for fast neural volume rendering", *Conference on Computer Vision and Pattern Recognition (CVPR)*, 2021. [1, 2, 6, 8](#).

[18] Thomas Neff, Pascal Stadlbauer, Mathias Parger, Andreas Kurz, Joerg H. Mueller, Chakravarty R. Alla Chaitanya, Anton Kaplanyan, and Markus Steinberger, "DONERF: Towards real-time rendering of compact neural radiance fields using depth oracle networks", *Eurographics Symposium on Rendering Techniques (EGSR)*, 2021. [2, 3, 5, 8](#).

[19] Stephan J. Garbin, Marek Kowalski, Matthew Johnson, Jamie Shotton, and Julien Valentin, "FastNeRF: High-fidelity neural rendering at 200FPS", *International Conference on Computer Vision (ICCV)*, 2021. [2, 6, 8](#).

[20] Christian Reiser, Songyou Peng, Yiyi Liao, and Andreas Geiger, "KiloNeRF: Speeding up neural radiance fields with thousands of tiny MLPs", *International Conference on Computer Vision (ICCV)*, 2021. [2, 6, 8](#).

[21] Kangle Deng, Andrew Liu, Jun-Yan Zhu, and Deva Ramanan, "Depth-supervised NeRF: Fewer views and faster training for free", *Conference on Computer Vision and Pattern Recognition (CVPR)*, 2022. [2, 6](#).

[22] Cheng Sun, Min Sun, and Hwann-Tzong Chen, "Direct voxel grid optimization: Super-fast convergence for radiance fields reconstruction", *Conference on Computer Vision and Pattern Recognition (CVPR)*, 2022. [2, 8](#).

[23] Sergio Boixo, Sergei V. Isakov, Vadim N. Smelyanskiy, Ryan Babbush, Nan Ding, Zhang Jiang, Michael J. Bremner, John M. Martinis, and Hartmut Neven, "Characterizing quantum supremacy in near-term devices", *Nature Physics*, vol. 14, no. 6, pp. 595-600, 2018. [2](#).

[24] Carlo Ciliberto, Mark Herbster, Alessandro Davide Ialongo, Massimiliano Pontil, Andrea Rocchetto, Simone Severini, and Leonard Wossnig, "Quantum machine learning: a classical perspective", *The Royal Society*, 2017. [2](#).

[25] Istvan Barabasi, Charles C. Tappert, Daniel Evans, and Avery M. Leider, "Quantum computing and deep learning working together to solve optimization problems", *International Conference on Computational Science and Computational Intelligence (CSCI)*, 2019. [3](#).

[26] Maria Schuld, "Supervised quantum machine learning models are kernel methods", *arXiv:2101.11020*, 2021. [3](#).

[27] Iordanis Kerenidis, and Alessandro Luongo, "Quantum classification of the MNIST dataset via Slow Feature Analysis", *arXiv:1805.08837*, 2018. [3](#).

[28] Danial Dervovic, Mark Herbster, Peter Mountney, Simone Severini, Naiři Usher, and Leonard Wossnig, "Quantum linear systems algorithms: a primer", *arXiv:1802.08227*, 2018. [3](#).

[29] Zhikuan Zhao, Jack K. Fitzsimons, Patrick Rebentrost, Vedran Dunjko, and Joseph F. Fitzsimons, "Smooth input

preparation for quantum and quantum-inspired machine learning", *arXiv:1804.00281*, 2018. 3.

[30] E. Miles Stoudenmire, and David J. Schwab, "Supervised learning with tensor networks", *Neural Information Processing Systems (NeurIPS)*, 2016. 3.

[31] Edward Grant, Marcello Benedetti, Shuxiang Cao, Andrew Hallam, Joshua Lockhart, Vid Stojovic, Andrew G. Green, and Simone Severini, "Hierarchical quantum classifiers", *npj Quantum Information*, vol. 4, pp. 1–8, 2018. 3.

[32] Shuxiang Cao, Leonard Wossnig, Brian Vlastakis, Peter Leek, and Edward Grant, "Cost function embedding and dataset encoding for machine learning with parameterized quantum circuits", *arXiv:1910.03902*, 2019. 3.

[33] Lov K. Grover, "Quantum mechanics helps in searching for a needle in a Haystack", *Physical Review Letters*, 1997. 5, 7.

[34] Ziwei Liu, Ping Luo, Xiaogang Wang and Xiaoou Tang, "Deep learning face attributes in the wild", *International Conference on Computer Vision (ICCV)*, 2015. 6, 7.

[35] Andrey Ignatov, Radu Timofte, et al., "PIRM challenge on perceptual image enhancement on smartphones", *European Conference on Computer Vision (ECCV) Workshops*, 2018. 6, 7.

[36] Arno Knapitsch, Jaesik Park, Qian-Yi Zhou, and Vladlen Koltun, "Tanks and temples: Benchmarking large-scale scene reconstruction", *ACM Trans. on Graphics*, 2017. 6, 8.

[37] Zhou Wang, Alan C. Bovik, Hamid R. Sheikh and Eero P. Simoncelli, "Image quality assessment: from error visibility to structural similarity", *IEEE Transactions on Image Processing*, 2004. 6.

[38] Richard Zhang, Phillip Isola, Alexei A Efros, Eli Shechtman and Oliver Wang, "The unreasonable effectiveness of deep features as a perceptual metric", *Conference on Computer Vision and Pattern Recognition (CVPR)*, 2018. 6.

[39] Sukin Sim, Peter D. Johnson, and Alan Aspuru-Guzik, "Expressibility and entangling capability of parameterized quantum circuits for hybrid quantum-classical algorithms", *arXiv:1905.10876*, 2019. 7.

[40] Maria Schuld and Nathan Killoran, "Quantum machine learning in feature hilbert spaces", *Physical Review Letters*, 122(4):040504, 2019. 4.

[41] Ryan LaRose and Brian Coyle, "Robust data encodings for quantum classifiers", *Physical Review A*, 2020. 4.

[42] Luca Parisi, Daniel Neagu, Renfei Ma and Felician Campean, "QReLU and m-QReLU: Two novel quantum activation functions to aid medical diagnostics", *arXiv:2010.08031*, 2020. 5.

Supplemental Material

Quantum Radiance Fields: A Quantum-Powered Photorealistic Rendering

We provide additional implementation details, discussions, and experimental results in the supplementary material to provide more detailed results and algorithms. In Section 1, we discuss the limitations and societal impact of our paper. In Section 2, we present the derivation details, including encoding circuit, quantum circuit, Grover algorithm, and optimization. Finally, we show the detailed quantitative and qualitative results on each scene in the additional experiments.

1. Discussion

1.1. Limitations

In deep learning, it is very useful to transform data into a higher-dimensional feature space. In the same way, there are two strategies for using quantum circuits to generate higher dimensional features: entangling more and more qubits. However, quantum computers are now in their infancy, the available qubits are limited. In this paper, we use photonic quantum computer with 216 squeezed-state qubits to construct our QRF. While inference is fast, the training time is longer than on a classical computer in the case of qubit limitation.

In addition, QRF and NeRFs are unable to sample the volume to infinity and instead assume that the scene lies between a near and far bound due to practical constraints. To ensure efficient execution of volume rendering, we treat the furthest radiance as an opaque wall for boundary limitation.

1.2. Societal Impact

QRF is a technique which empowers NeRFs to operate on a variety of scenes. While novel view synthesis is not a synthetic media, it can open the door to abuse when generating face image through the scene. There could also be privacy concerns, as using QRF technology to better render the sharper details of a face could capture personally identifiable information.

Significant drawbacks with the technology of QRF and NeRFs are concerns surrounding privacy. For example, the specific face rendering and recognition technology used, how it's deployed, and what computing method it relies on all play a part in determining how much of a privacy risk it is. These worries about privacy aren't unreasonable. People don't like to feel they're being watched or that personal information could be leaked. These anxieties are reflected by institutions worldwide that have implemented strict regulations to protect people's biometric data. Europe's General Data Protection Regulation (GDPR) [1]

is an example of this. Europe's GDPR details that citizens are entitled to their privacy and that any breach of privacy will be met with consequences.

Whether we are delivering the NeRFs app or user experience directly to consumers or any company, we require appropriate notification. This means that consumers are very aware of the personally identifiable data we will be collecting.

2. Derivation Details

We present the encoding circuit, quantum logic gate, and our proposed detail quantum circuits, then we introduce the Grover algorithm for calculating numerical integrals in this paper.

2.1. Encoding Circuit

The encoding circuit is used to encode the classical data into the physical states of Hilbert space for quantum computing. In this section, we introduce another 3 encoding methods [2] applied in the paper, including General Qubit Encoding, Wavefunction Encoding, Angle Encoding.

General Qubit Encoding. In this encoding, the data has to be in form of a binary string to get encoding. Approximating a scalar value to its binary form and then transforming it to a quantum state. For example, if we have a classical dataset containing two examples $x_k = 01$ and $x_{k+1} = 11$, the corresponding quantum state after basis encoding is $|x_k\rangle = |01\rangle$ and $|x_{k+1}\rangle = |11\rangle$. In short, Basis encoding encodes an n-bit binary string x_k to an n -qubit quantum state as:

$$|x_k\rangle = |i_x\rangle \quad (1)$$

where $|i_x\rangle$ is a computational basis state, and every binary string has a unique integer representation $i_x = \sum_{k=0}^{n-1} 2^k x_k$.

Wavefunction Encoding. The wavefunction encoding is also known as amplitude embedding. The amplitude is the height of a wave. In this encoding, the data points are transformed into amplitudes of the quantum state. A normalized classical N -dimensional x_k is represented by the amplitudes of a n -qubit quantum state $|x_k\rangle$ as:

$$|x_k\rangle = \sum_{k=0}^N x_k |i_x\rangle \quad (2)$$

where N is the length of vector x_k into amplitudes of an n -qubit quantum state with $n = \log_2(N)$. $\{|i_x\rangle\}$ is the

computational basis for the Hilbert space. Since the classical information forms the amplitudes of a quantum state, the input needs to satisfy the normalization condition: $|x|^2 = 1$.

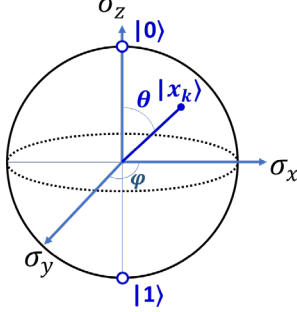


Figure 1: Angle encoding with a rotation angle of θ around z -axis on the Hilbert space.

Angle Encoding. Angle encoding makes use of rotation gates to encode classical information $x_k \in \mathbb{R}^N$ without any normalization condition. The classical information determines angles of rotation gates:

$$|x_k\rangle = \otimes_{k=0}^N R(x_k)|0^N\rangle \quad (3)$$

Where N is the number of qubits, R can be one of R_x , R_y , R_z . Usually, N used for encoding is equal to the dimension of vector x_k . Since it is 2π -periodic one may want to limit \mathbb{R}^N to the hypercube $[0, 2\pi]^{\otimes n}$. The i -th feature x_k is encoded into the k -th qubit via a Pauli-X rotation. Figure 1 show the angle encoding with a rotation angle of θ around z -axis on the Hilbert space.

After activation function $\tanh(x)$, the output $x_k \in [-1, 1]$ from the end of classical layer. Then, the rotation angle is mapped between $\theta \in [0, \pi]$ due to the periodicity of the cosine function. This is relevant since the expectation value is taken with respect to the σ_z operator at

the end of the circuit execution.

2.2. Quantum Logic Gate

Quantum logical gate is used in quantum computing, which is essentially a transformation of one or more qubits. We have given a description of the quantum gate types in Figure 2.

CNOT Gate means the quantum logic gate which acts on a pair of qubits by the linear map which is given in this way on the canonical linear basis-elements of a pair of qubits, where the first qubit is usually referred to as the control qubit and the second qubit as the target qubit. Expressed in basis states, the CNOT gate:

(1) leaves the control qubit unchanged and performs a Pauli-X gate on the target qubit when the control qubit is in state $|1\rangle$.

(2) leaves the target qubit unchanged when the control qubit is in state $|0\rangle$.

Rotation Gate give rise to the rotation operators, which rotate the Bloch vector about the x, y and z axes, by a given angle θ :

$$R_x(\theta) = e^{-i\frac{\theta}{2}\sigma_x}, R_y(\theta) = e^{-i\frac{\theta}{2}\sigma_y}, R_z(\theta) = e^{-i\frac{\theta}{2}\sigma_z} \quad (4)$$

Now, if an operator A satisfies $A^2 = I$, it can be shown that:

$$e^{i\theta A} = \cos(\theta)I + i \sin(\theta)A \quad (5)$$

And since all the Pauli matrices satisfy $X^2 + Y^2 + Z^2 = I$, the rotation operator can be expanded as:

$$\begin{aligned} R_x(\theta) &= e^{-i\frac{\theta}{2}\sigma_x} = \cos\left(\frac{\theta}{2}\right)I - i \sin\left(\frac{\theta}{2}\right)\begin{bmatrix} 0 & 1 \\ 1 & 0 \end{bmatrix} \\ &= \begin{bmatrix} \cos(\theta/2) & -i\sin(\theta/2) \\ -i\sin(\theta/2) & \cos(\theta/2) \end{bmatrix} \end{aligned} \quad (6)$$

Quantum Gate	the number of qubit	Symbol	Matrix	Description
CNOT	2 qubit		$\begin{bmatrix} 1 & 0 & 0 & 0 \\ 0 & 1 & 0 & 0 \\ 0 & 0 & 0 & 1 \\ 0 & 0 & 1 & 0 \end{bmatrix}$	Used to measure 2 nd qubit
Rotation Gate-X	1 qubit		$\begin{bmatrix} \cos(\theta/2) & -i\sin(\theta/2) \\ -i\sin(\theta/2) & \cos(\theta/2) \end{bmatrix}$	Create x rotation with θ
Rotation Gate-Y	1 qubit		$\begin{bmatrix} \cos(\theta/2) & -\sin(\theta/2) \\ \sin(\theta/2) & \cos(\theta/2) \end{bmatrix}$	Create y rotation with θ
Rotation Gate-Z	1 qubit		$\begin{bmatrix} \cos(\theta/2) & -i\sin(\theta/2) & 0 \\ 0 & \cos(\theta/2) + i\sin(\theta/2) & 0 \\ 0 & 0 & 1 \end{bmatrix}$	Create z rotation with θ

Figure 2: Quantum Logic Gates

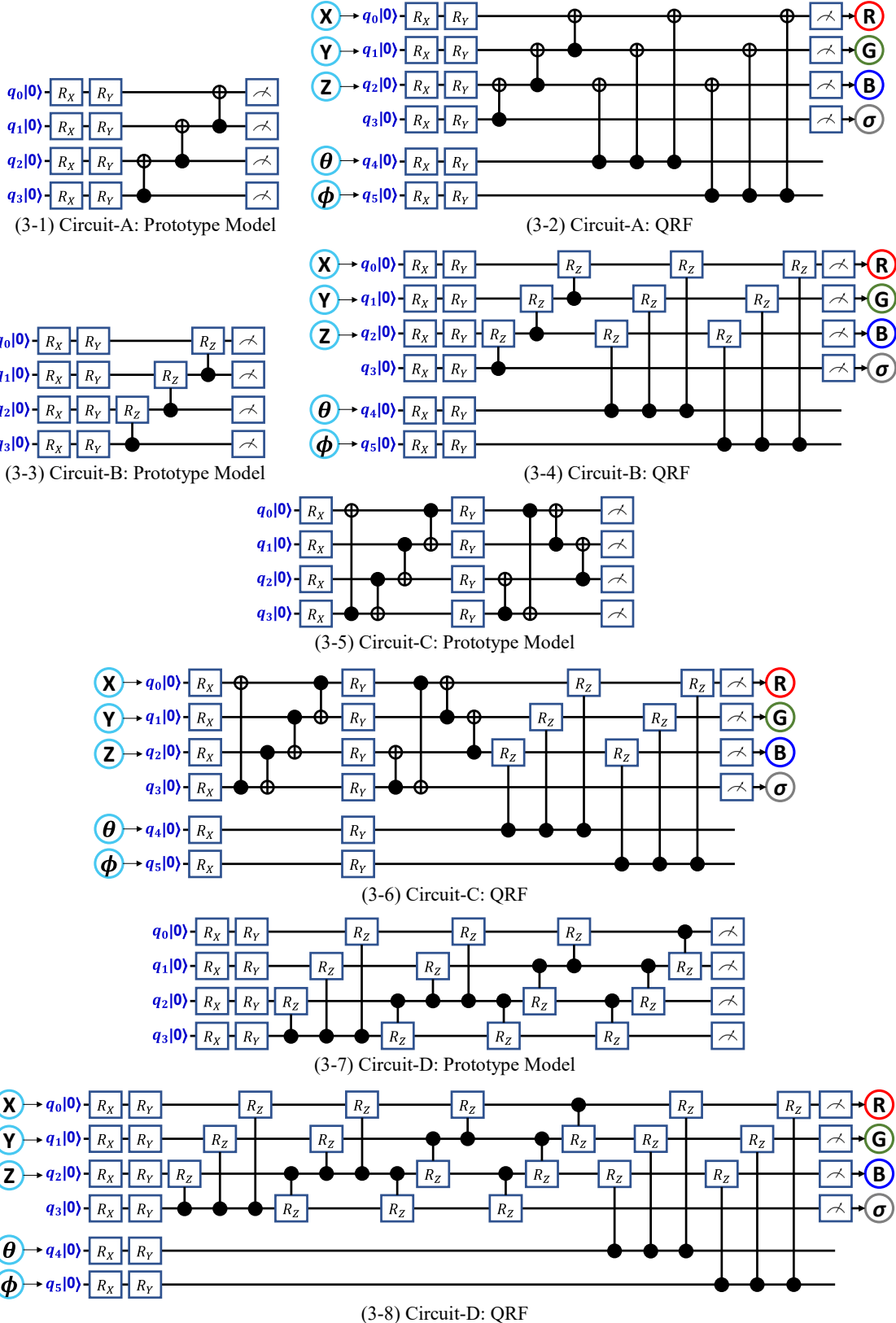


Figure 3: Quantum Circuit from prototype model (3-1, 3-3, 3-5, 3-7) [3][4] and its' extend model of Quantum Radiance Fields (3-2, 3-4, 3-6, 3-8). Similar to the architecture of NeRF [5], QRF enforces that the predicted σ is independent of view direction.

$$\begin{aligned}
R_y(\theta) &= e^{-i\frac{\theta}{2}\sigma_y} = \cos\left(\frac{\theta}{2}\right)I - i \sin\left(\frac{\theta}{2}\right) \begin{bmatrix} 0 & -i \\ i & 0 \end{bmatrix} \\
&= \begin{bmatrix} \cos(\theta/2) & -\sin(\theta/2) \\ \sin(\theta/2) & \cos(\theta/2) \end{bmatrix} \quad (7)
\end{aligned}$$

$$\begin{aligned}
R_z(\theta) &= e^{-i\frac{\theta}{2}\sigma_z} = \cos\left(\frac{\theta}{2}\right)I - i \sin\left(\frac{\theta}{2}\right) \begin{bmatrix} 1 & 0 \\ 0 & -1 \end{bmatrix} \\
&= \begin{bmatrix} \cos(\theta/2) & -i\sin(\theta/2) & 0 \\ 0 & \cos(\theta/2) & i\sin(\theta/2) \end{bmatrix} \quad (8)
\end{aligned}$$

2.3. Quantum Circuit

Quantum circuit is a system comprising multiple qubits. A quantum computer stores its quantum data in one or more quantum circuits. We use circuit-A/B/C by Paulo Sousa et al. [3] and circuit-D by Maria Schuld et al. [4] as baselines for quantum circuits (as shown in Figure 3).

Figure 3-1, 3-3, 3-5, 3-7 is the prototype model by Paulo Sousa et al. and circuit-D by Maria Schuld et al., and Figure 3-2, 3-4, 3-6, 3-7 is the extend of Quantum Radiance Fields. CNOT gates, rotation gates are used to construct our quantum circuit. For input, 3D position (x, y, z) and viewing direction (θ, ϕ) are encoded by dense angle encoding, and it output colors (r, g, b) and transparency values (σ). Similar to the NeRF [5], QRF enforces that the predicted σ is independent of view direction. Therefore, we do not perform any cross quantum operation on 4th qubit (q_3) and 5th/6th qubit (q_4, q_5). Finally, we perform the measurement on $q_0/q_1/q_2/q_3$, mapping a quantum state to a classical vector, to get the final result (colors and transparency values).

2.4. Grover Search

Rendering on conventional computers is capable of generating realistic imagery, but the computational complexity of these light transport algorithms is a limiting. The main problem that needs to be addressed is supersampling of the image, which can be seen as a mean estimation per pixel. Grover algorithm [6,7] was the first to introduce a quantum algorithm for estimating a mean. The idea is to combine Amplitude Amplification (AA) with Quantum Fourier Transformation (QFT). Johnston [8] first implemented Grover algorithm to conduct numerical integrations in the context of rendering. Volume rendering is essentially a numerical integration problem in each pixel, which is commonly done by Monte Carlo integration on classical computers. In this paper, we apply Grover algorithm to design a ray tracing oracle for volume rendering.

The main idea of Grover algorithm is to exploit the existence of a periodic cycle when we keep applying amplitude amplification on $|\psi\rangle$. Applying QFT on the history of rotated $|\psi\rangle$, we can extract the frequency of this

periodic cycle, which then allows us to calculate the corresponding $|\psi\rangle$. Given a function $F(a) : a \rightarrow [0,1]$ and a quantum oracle operator:

$$\widehat{Q}_F = |0\rangle \otimes |i\rangle \rightarrow (\sqrt{1-F(i)}|0\rangle + \sqrt{F(i)}|1\rangle) \otimes |i\rangle \quad (9)$$

where the objective is to get the average f of $F(a)$ with N samples: $\frac{1}{N} \sum_{j=0}^{N-1} f(j)$. we use the oracle \widehat{Q}_F and make a superposition state $|\psi_0\rangle$ from the initial state whose all qubits are $|0\rangle$, where the numbers of qubits for each are $\log_2 P, 1, \log_2 N$. We thus write the initial state as

$$|0 \dots 0\rangle \otimes |0\rangle \otimes |0 \dots 0\rangle = |0\rangle \otimes |0\rangle \otimes |0\rangle \quad (10)$$

We generate a superposition state $|\psi_0\rangle$ as

$$\begin{aligned}
|\psi_0\rangle &= \widehat{Q}_F(\widehat{H} \otimes \widehat{I} \otimes \widehat{H})|0\rangle \otimes |0\rangle \otimes |0\rangle \\
&= \frac{1}{\sqrt{PN}} \sum_{m=0}^{P-1} \sum_{i=0}^N |m\rangle \otimes \widehat{Q}_F(|0\rangle \otimes |i\rangle) \\
&= \frac{1}{\sqrt{PN}} \sum_{m=0}^{P-1} \sum_{i=0}^N |m\rangle \otimes (\sqrt{1-F(i)}|0\rangle + \sqrt{F(i)}|1\rangle) \otimes |i\rangle
\end{aligned} \quad (11)$$

We can define $\cos(\theta)$ and $\sin(\theta)$ as $\sqrt{1-F(i)}$ and $\sqrt{F(i)}$, and $|\psi_0\rangle$ is:

$$|\psi_0\rangle = \frac{1}{\sqrt{P}} \sum_{m=0}^{P-1} |m\rangle \otimes (\cos \theta |0\rangle + \sin \theta |1\rangle) \otimes |i\rangle \quad (12)$$

We then apply Amplitude Amplification to the $\cos \theta |0\rangle + \sin \theta |1\rangle$ state for P times:

$$\begin{aligned}
|\psi_1\rangle &= \frac{1}{\sqrt{P}} \sum_{m=0}^{P-1} |m\rangle \otimes (\cos(2m+1) |0\rangle \\
&\quad + \sin(2m+1) |1\rangle) \otimes |i\rangle
\end{aligned} \quad (13)$$

We then measure the target qubits and assume that the state is converged to $|1\rangle$:

$$|\psi_2\rangle = \frac{1}{C} \sum_{m=0}^{P-1} \sin(2m+1) \theta |m\rangle |1\rangle \quad (14)$$

Finally, we perform QFT on $|\psi_2\rangle$. With a sufficiently large probability, the result of measurement will be:

$$t \simeq \frac{P\theta}{\pi}, \frac{P(\pi-\theta)}{\pi} \quad (15)$$

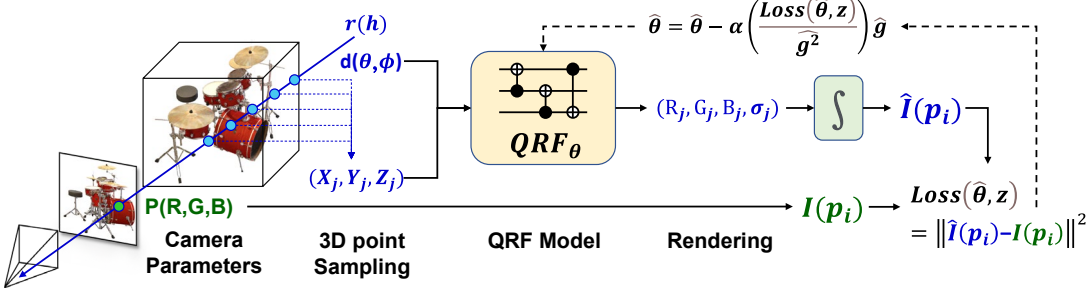


Figure 4: Quantum Radiance Fields Optimization. We supervise our QRF model by gradient descent using a simple $L2$ loss:

If the measured and converged state is $|0\rangle$, we get the same result. Therefore, we can deduce the estimated average f by:

$$f' \approx \sin^2\left(\frac{t\pi}{P}\right) \quad (16)$$

Since $\frac{t\pi}{P}$ can be determined by the precision $O(1/P)$ in this process, f' also has the precision of $O(1/P)$. The estimation error $|f - f'|$ is inversely proportional to the number of Amplitude Amplification operations P . Since Amplitude Amplification uses two queries per operation, we perform $O(N)$ queries to achieve $O(1/N)$ error. Note that this convergence rate is faster than $O(1/\sqrt{N})$ of Monte Carlo integration.

2.5. Optimization

In the Quantum Radiance Fields, the scene is represented by a Parametrized Quantum Circuits PQC_θ with parameter θ_n to capture the volume 3D representation. QRF's model $PQC_\theta: (p, d) \rightarrow (c, \sigma)$ maps 3D position $p \in \mathbb{R}^3$ and light direction $d \in \mathbb{R}^2$ to color value c and transparency σ (as shown in Figure 4). The architecture of PQC_θ is chosen such that only the color c depends on the viewing direction d . This encourages the learning of consistent geometry. In the deterministic preprocessing step, x and d are transformed via a positional encoding γ , which promotes the learning of high frequency details. To render a single image pixel, a ray is cast from the center of the camera, through that pixel and into the scene. We denote the direction of this ray as d . Multiple 3D positions (p_1, \dots, p_k) are then sampled along the ray between the near and far boundaries defined by the camera parameters. The PQC_θ is evaluated at each position p_i and ray direction d to produce color c_i and transparency σ_i . These intermediate outputs are then integrated as follows to produce the final pixel color \hat{c} :

$$\hat{c} = \sum_i^K T_i (1 - e^{(-\sigma_i \delta_i)}) c_i \quad (17)$$

where $T_i = e^{-\sum_{j=1}^{i-1} \sigma_j \delta_j}$ is the transmittance and $\delta_j = (p_{i+1} - p_i)$ is the distance between samples.

QRF is trained by minimizing a photometric loss between rendered images and training images. More specifically, for each parameter update step, we randomly sample a training image and N pixels $p_i \in (c_1, \dots, c_N)$ inside that image. Subsequently, the corresponding pixels $\hat{p}_i \in (\hat{c}_1, \dots, \hat{c}_N)$ are rendered according to Eq. 17. As shown in Figure 4, the model parameters θ are optimized by minimizing an $L2$ reconstruction loss between the rendered pixels and their ground truth:

$$Loss = \sum_{i=1}^N \|\hat{p}_i - p_i\|^2 \quad (17)$$

The quantum processor implements unitary transformations on input states. We have a set of basic unitaries $\{U_\alpha(\theta)\}$. The input state $|\psi, 1\rangle$ is prepared and then transformed via a sequence of few qubit unitaries $U_\alpha(\theta_i)$ that depend on parameters θ_i . These (θ_i) get adjusted during learning such that the measurement on the readout qubit tends to produce the desired label for $|\psi\rangle$. Our goal is to find parameters $\hat{\theta}$ so that the predicted render color \hat{c}_i is near the true label. We will address the question of whether such parameters even exist as well as the question of whether such optimal parameters can then be efficiently found. For a given circuit, a set of parameters $\hat{\theta}$, and an input string (p, d) , consider the sample loss:

$$Loss = 1 - \langle (p, d), 1 | U'(\hat{\theta})(c, \sigma) U(\hat{\theta}) | (p, d), 1 \rangle \quad (18)$$

Consider the derivative of the sample loss (as Eq. 18) with respect to θ_k which is associated with the unitary $U_\alpha(\theta_k)$ which has the generalized Pauli operator $\sum k$. Now:

$$\frac{dLoss(\hat{\theta}, z)}{d\theta_k} = 2Im(\langle z, 1 | U'(\hat{\theta}) Y_{n+1} U(\hat{\theta}) | z, 1 \rangle) \quad (19)$$

where $z = (p, d)$ is the input of PQC, $Y_{n+1} = (c, \sigma)$ is the prediction after measurement. Given an accurate estimate

of the gradient we need a strategy for how to update $\hat{\theta}$. Let \hat{g} be the gradient of $Loss(\hat{\theta}, z)$ with respect to $\hat{\theta}$. Now we want to change $\hat{\theta}$ in the direction of \hat{g} . To lowest order in γ we have that:

$$Loss(\hat{\theta} + \gamma \hat{g}, z) = Loss(\hat{\theta}, z) + \gamma \hat{g}^2 + \mathcal{O}(\gamma^2) \quad (20)$$

We want to move the loss to its minimum at 0 so the first thought is to make $\gamma = -\frac{Loss(\hat{\theta}, z)}{\hat{g}^2}$, then introduce a learning rate α and apply the basic gradient descent rule:

$$\hat{\theta} = \hat{\theta} - \alpha \left(\frac{Loss(\hat{\theta}, z)}{\hat{g}^2} \right) \hat{g} \quad (21)$$

We use Adam optimizer with a learning rate parameter α to keep track of gradient moments over time to redirect the optimization trajectory.

3. Additional Experiments

Quantitative Results. We present the per-scene quantitative comparisons in Table 1 for three dataset: Synthetic-NeRF [9], Synthetic-NSVF [10], Tanks and Temples [11]. We adopt PSNR as the evaluation metric. QRF perform the best result to most of the recent methods, except the JaxNeRF [14] and NSVF [10]. Moreover, all the methods after NeRF on the tables take quite a few minutes to inference for each scene, while our method only takes about few seconds for volume rendering.

Qualitative Results. We provide more qualitative results in Figure 5 for Synthetic-NeRF [9], Figure 6 for Synthetic-NSVF [10], and Figure 7 for Tanks and Temples [11]. In Figure 5, we compare our results with the original NeRF implementation [9], Neural Sparse Voxel Field (NSVF) [10], AutoInt [15], DoNeRF [16], FastNeRF [17], and KioNeRF [18] on Synthetic-NeRF [9] dataset. In Figure 6, we show our QRF qualitative results on 8 scenes of Synthetic-NSVF [10]. In Figure 7, we show our QRF qualitative results on 4 scenes of Tanks and Temples [11].

Figures 8/9/10 show the inference results after training QRF with 70k iterations on our own 3 datasets: Succulents, Model of Eluanbi Lighthouse, and Bench in Bade Daming Park, respectively.

References

- [1] Ben Wolford, "What is GDPR, the EU's new data protection law?", *GDPR.EU*, 2020, <https://gdpr.eu/what-is-gdpr/>. 1.
- [2] YuanFu Yang and Min Sun, "Semiconductor Defect Detection by Hybrid Classical-Quantum Deep Learning", *Conference on Computer Vision and Pattern Recognition (CVPR)*, pp. 2313-2322, 2022. 1.
- [3] Paulo B. Sousa and Rubens V. Ramos, "Universal quantum circuit for n-qubit quantum gate: A programmable quantum gate", *arXiv:quant-ph/0602174*, 2006. 3, 4.
- [4] Maria Schuld, Alex Bocharov, Krysta Svore, Nathan Wiebe, "Circuit-centric quantum classifiers", *arXiv:1804.00633*, 2018. 3, 4.
- [5] Ben Mildenhall, Pratul P. Srinivasan, Matthew Tancik, Jonathan T. Barron, Ravi Ramamoorthi and Ren Ng, "NeRF: representing scenes as neural radiance fields for view synthesis", *European Conference on Computer Vision (ECCV)*, 2020. 3, 4.
- [6] Lov K. Grover, "Quantum mechanics helps in searching for a needle in a haystack", *Physical Review Letters*, 1997. 4.
- [7] Maria Schuld and Nathan Killoran, "Quantum machine, learning in feature hilbert spaces", *Physical Review Letters*, 122(4):040504, 2019. 4.
- [8] Eric R. Johnston r, "Quantum supersampling", *ACM SIGGRAPH*, 2016. 4.
- [9] Ben Mildenhall, Pratul P. Srinivasan, Matthew Tancik, Jonathan T. Barron, Ravi Ramamoorthi and Ren Ng, "NeRF: representing scenes as neural radiance fields for view synthesis", *European Conference on Computer Vision (ECCV)*, 2020. 6, 7, 8.
- [10] Lingjie Liu, Jitao Gu, Kyaw Zaw Lin, Tat-Seng Chua and Christian Theobalt, "Neural sparse voxel fields", *Neural Information Processing Systems (NeurIPS)*, 2020. 6, 7, 9.
- [11] Arno Knapitsch, Jaesik Park, Qian-Yi Zhou, and Vladlen Koltun, "Tanks and temples: Benchmarking large-scale scene reconstruction", *ACM Trans. on Graphics*, 2017. 6, 7, 10.
- [12] Vincent Sitzmann, Michael Zollhöfer and Gordon Wetzstein, "Scene representation networks: Continuous 3d-structure-aware neural scene representations", *Neural Information Processing Systems (NeurIPS)*, 2019. 6.
- [13] Stephen Lombardi, Tomas Simon, Jason Saragih, Gabriel Schwartz, Andreas Lehrmann and Yaser Sheikh, "Neural volumes: Learning dynamic renderable volumes from images", *ACM Transactions on Graphics (TOG)*, vol. 38, no. 4, pp. 65-65, 2019. 6.
- [14] Boyang Deng, Jonathan T. Barron, and Pratul P. Srinivasan, "JaxNeRF: an efficient JAX implementation of NeRF", 2020. 6.
- [15] David B. Lindell, Julien N. P. Martel, and Gordon Wetzstein, "AutoInt: Automatic integration for fast neural volume rendering", *Conference on Computer Vision and Pattern Recognition (CVPR)*, 2021. 6.
- [16] Thomas Neff, Pascal Stadlbauer, Mathias Parger, Andreas Kurz, Joerg H. Mueller, Chakravarty R. Alla Chaitanya, Anton Kaplanyan, and Markus Steinberger, "DOneRF: Towards real-time rendering of compact neural radiance fields using depth oracle networks", *Eurographics Symposium on Rendering Techniques (EGSR)*, 2021. 6.
- [17] Stephan J. Garbin, Marek Kowalski, Matthew Johnson, Jamie Shotton, and Julien Valentin, "FastNeRF: High-fidelity neural rendering at 200FPS", *International Conference on Computer Vision (ICCV)*, 2021. 6.
- [18] Christian Reiser, Songyou Peng, Yiyi Liao, and Andreas Geiger, "KiloNeRF: Speeding up neural radiance fields with thousands of tiny MLPs", *International Conference on Computer Vision (ICCV)*, 2021. 6.

Table 1: Quantitative results on each scene from the Synthetic-NeRF [9], Synthetic-NSVF [10], and Tanks and Temples [11]. We highlight the top 3 results in each column are color coded as **Top 1**, **Top 2** and **Top 3**.

Synthetic-NeRF [9]									
Scenes	Avg.	Chair	Ship	Hotdog	Drums	Ficus	Materials	Lego	Mic
SRN [12]	22.26	26.82	20.67	26.78	17.14	20.85	18.03	20.96	26.79
Neural Volumes [13]	26.05	28.21	23.79	30.58	22.53	25.14	24.33	26.10	27.73
NeRF [9]	31.01	33.05	28.60	35.16	25.34	30.37	29.67	32.17	33.73
JaxNeRF [14]	31.69	35.49	29.55	34.98	25.37	30.84	29.90	33.69	33.72
NSVF [10]	31.75	33.21	27.91	37.16	25.16	31.25	32.66	32.31	34.35
AutoInt [15]	25.55	25.14	22.12	30.14	20.57	22.50	25.38	31.14	27.38
DoNeRF [16]	32.50	35.17	30.44	37.73	25.65	30.15	31.29	35.17	34.42
FastNeRF [17]	29.97	32.43	27.88	34.79	23.74	27.80	28.94	32.41	31.76
KioNeRF [18]	31.00		28.85	35.99	24.56	28.76	29.94	33.52	32.85
QRF	32.65	35.34	30.35	37.96	25.87	30.29	31.51	35.30	34.57
Synthetic-NSVF [10]									
Scenes	Avg.	Bikes	Wineholder	Spaceship	Streamtrain	Palace	Lifestyle	Toad	Robot
SRN [12]	24.33	23.79	20.71	27.95	25.53	24.46	24.57	25.35	22.28
Neural Volumes [13]	25.83	26.64	21.33	29.92	25.30	26.37	27.69	24.62	24.75
NeRF [9]	30.81	31.76	28.24	34.69	30.82	31.75	31.09	29.44	28.70
JaxNeRF [14]	31.49	32.46	28.86	35.46	31.50	32.45	31.78	30.09	29.33
NSVF [10]	35.18	37.56	32.45	39.12	33.11	34.41	35.92	33.41	35.48
AutoInt [15]	26.63	28.43	24.34	29.61	26.58	25.82	26.28	25.21	26.78
DoNeRF [16]	32.29	34.47	29.51	35.91	32.23	31.31	31.87	30.57	32.47
FastNeRF [17]	29.78	31.79	27.22	33.12	29.72	28.87	29.39	28.20	29.95
KioNeRF [18]	33.37	35.63	30.50	37.11	33.30	32.36	32.93	31.60	33.56
QRF	35.44	37.84	32.39	39.41	35.37	34.36	34.98	33.56	35.64
Tanks and Temples [11]									
Scenes	Avg.	Family	Barn	Truck	Caterpillar	Ignatius	-	-	-
SRN [12]	24.10	27.55	22.42	22.65	21.15	26.71	-	-	-
Neural Volumes [13]	23.70	27.73	21.69	21.39	21.57	26.14	-	-	-
NeRF [9]	25.78	30.25	24.11	24.58	23.66	26.30	-	-	-
JaxNeRF [14]	27.94	32.48	27.38	26.65	25.21	27.96	-	-	-
NSVF [10]	28.42	33.58	27.17	26.95	26.46	27.92	-	-	-
AutoInt [15]	22.28	26.33	21.30	21.13	20.74	21.89	-	-	-
DoNeRF [16]	27.02	31.93	25.83	25.62	25.16	26.54	-	-	-
FastNeRF [17]	24.92	29.44	23.82	23.63	23.20	24.48	-	-	-
KioNeRF [18]	28.41	33.57	27.16	26.94	26.45	27.91	-	-	-
QRF	29.65	35.03	28.35	28.12	27.61	29.13	-	-	-



Figure 5: Qualitative comparisons on Synthetic-NeRF [9].



Figure 6: Inference Result of QRF on Synthetic-NSVF [10].



Figure 7: Inference Result of QRF on Tanks and Temples [11].



Figure 8: Inference Result of QRF on our own dataset - Succulents

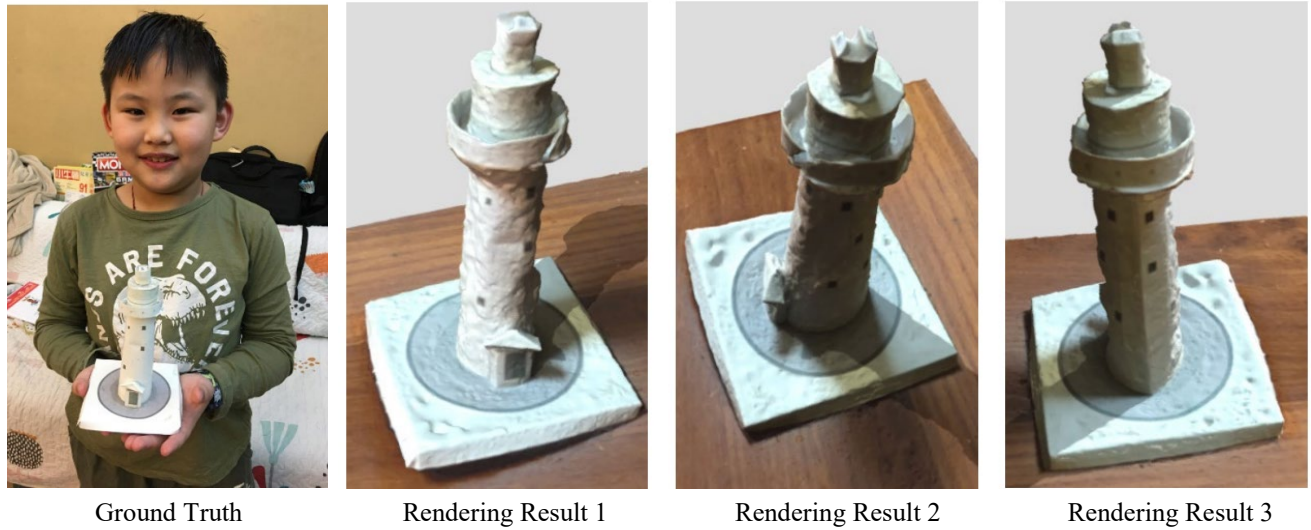


Figure 9: Inference Result of QRF on our own dataset - The model of Eluanbi Lighthouse

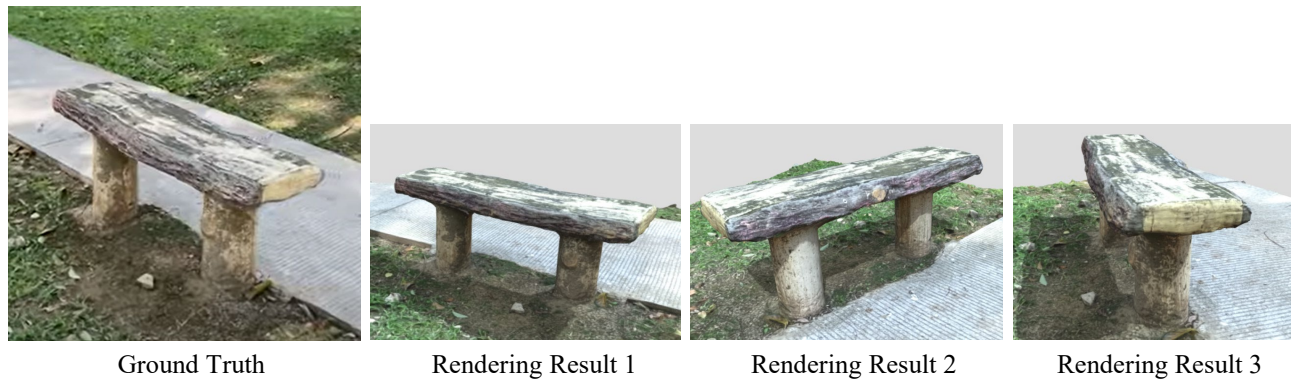


Figure 10: Inference Result of QRF on our own dataset - The bench in Daming Park.